From Natural Occulters to Programmable Pre-Aperture Coronagraphy for Ground-Based Direct Exoplanet Imaging

Brent Hartshorn

May 18, 2026

Abstract

Direct imaging of Earth-like exoplanets demands a contrast ratio of $\sim 10^{10}$—far beyond conventional ground-based coronagraphy. We present a unified atmospheric architecture that eliminates the need for a dedicated space observatory. Its centerpiece is the *Drone-Borne Synthetic Aperture Starshade* (DSAS): a multi-ring UAV formation at staggered altitudes, each ring suspending programmable electro-optical fabric that acts simultaneously as an adaptive occulting mask, a multi-plane Fresnel zone plate, and a distributed wavefront sensor. Real-time apodization via the Huygens-Fresnel integral, combined with an internal Optical Vortex Phase Mask (OVPM), is projected to deliver 10^{-10} contrast at the detector. As a complementary opportunistic channel, Trans-Neptunian Object (TNO) occultations observed near Radial-Velocity Stationary Points with pre-positioned linear telescope arrays convert rapid shadow transits into scientifically viable integration windows.

1 Introduction

Transit photometry and radial-velocity surveys have catalogued thousands of planetary candidates, but biosignature characterization requires direct photon detection from the planet itself. Two barriers stand in the way.

Contrast. A Sun-like star outshines an Earth-analog companion by $\sim 10^{10}$ in reflected light.

Diffraction. The stellar Airy pattern swamps any nearby faint source within a finite aperture.

Existing mitigations fall into two families: *internal coronagraphs*, which require sub-nanometer mirror polish and suffer speckle noise, and *space starshades*, which demand formation flying at separations of tens of thousands of kilometers. Both carry steep cost and engineering barriers.

We develop a third path: *pre-aperture engineering*, in which the starlight-suppression function is distributed across a redeployable, programmable atmospheric system above the telescope. The architecture has two synergistic elements described in Sections 2–3, followed by performance analysis in Section 4.

2 The Drone-Borne Synthetic Aperture Starshade

2.1 Physical Architecture

The DSAS consists of K concentric UAV rings at altitudes $h_1 < h_2 < \cdots < h_K$ above the telescope primary mirror. Ring k has N_k drones at equal angular intervals on a circle of radius R_k centered on the optical axis; adjacent drones suspend a lightweight electro-optical fabric panel, forming a continuous annular surface (Figure 1).

Each fabric panel serves three simultaneous functions: (1) *broadband occulting mask* — opaque at baseline, with spatially programmable transmittance $T(x, y, t) \in [0, 1]$ via an LCoS or electrochromic layer; (2) *Fresnel zone plate layer* — each ring radius R_k satisfies $R_k^2 = m_k \lambda h_k$ for selected zone order m_k; (3) *distributed Hartmann wavefront sensor* — embedded photodiodes sample the irradiance field $I(x_i, y_i, t)$.

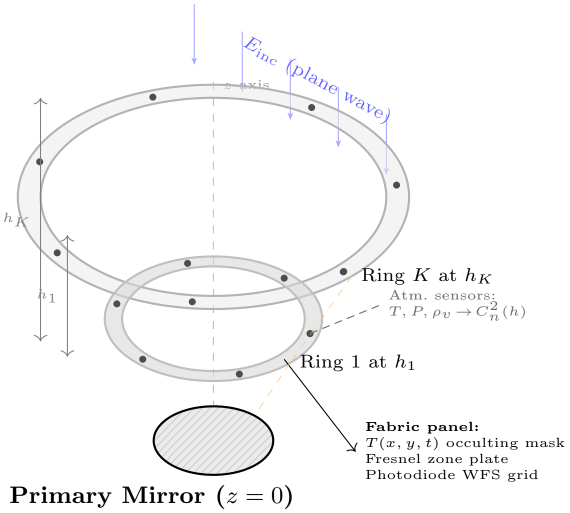

Figure 1: DSAS physical architecture. K UAV rings at staggered altitudes suspend programmable electro-optical fabric. Each ring functions simultaneously as an occulting mask, a Fresnel zone plate layer, and a distributed wavefront sensor.

Each UAV additionally carries a capacitive humidity sensor, a 3-axis ultrasonic anemometer, and a precision thermistor, giving a real-time volumetric $C_n^2(h)$ profile at all K altitudes.

UAV feasibility is grounded in recent demonstrations: Kuhn et al. (2025) [1] achieved centimeter-level DGPS positioning of drone formations above radio dish arrays; Brown et al. (2022) [2] showed UAV-borne calibration sources can operate near precision optical instruments without prohibitive contamination; Li et al. (2025) [3] validated drone payloads for large-aperture beam characterization.

2.2 Occulting Field and Apodization

With the z-axis along the star–telescope line of sight and the DSAS plane at altitude H, the field at the telescope entrance pupil is

$$E_{\text{tel}}(u, v) = \frac{e^{ikH}}{i\lambda H} \iint_{\mathbb{R}^2} \big[1 - T(x, y)\big]\, E_{\text{inc}}\, e^{\frac{ik}{2H}[(u-x)^2+(v-y)^2]}\, dx\, dy, \tag{1}$$

where $k = 2\pi/\lambda$. For a circularly symmetric ring (R_{in} to R_{out}) the on-axis suppression reduces to a Lommel-function integral in J_0. Choosing $T(r)$ to match a raised-cosine or hyper-Gaussian apodization drives the integral to zero to arbitrary order, and the real-time programmability of $T(x, y, t)$ allows this optimization to be recomputed at the drone telemetry cadence ($\sim$10 Hz) to compensate for fabric deformation, residual positioning error, and changing seeing.

2.3 Multi-Plane Fresnel Zone Plate

The novel contribution of the DSAS is using rings at *different altitudes* as a three-dimensional Fresnel zone plate—a geometry with no equivalent in single-plane starshade or internal coronagraph designs.

The m-th Fresnel zone radius at distance H is $r_m = \sqrt{m\lambda H}$. Ring k coincides with Fresnel zone m_k when

$$R_k^2 = m_k\, \lambda\, h_k. \tag{2}$$

The coherent on-axis field from ring k (treated as a narrow annulus of width δ_k) is

$$E_k(0) = \frac{k}{ih_k} \int_{R_k-\delta_k/2}^{R_k+\delta_k/2} T_k(r)\, e^{i\frac{kr^2}{2h_k}}\, r\, dr, \tag{3}$$

and the total telescope field is

$$E_{\text{total}} = E_{\text{free}} - \sum_{k=1}^{K} E_k^{\text{blocked}}. \tag{4}$$

Setting $E_{\text{total}} = 0$ on-axis requires $\sum_k E_k^{\text{blocked}} = E_{\text{free}}$.

The multi-plane geometry provides two advantages over single-plane zone plates: (i) the effective numerical aperture is set by the outermost ring radius R_K and total altitude span h_K, which can be made substantially larger than any single-plane structure; (ii) adjusting the altitude spacing Δh tunes the axial intensity distribution without altering ring radii, a degree of freedom unavailable to any planar optic.

Because Fresnel zone radii scale as $\sqrt{\lambda}$, broadband suppression requires the programmable transmittance $T_k(r, \lambda)$ to implement an achromatic correction across the full bandpass (Serabyn 2026) [4]. Multilevel diffractive techniques (Shi et al. 2024) [5] and (Zhang 2017) [6] applied to the fabric substrate provide a practical route to this achromatic performance; tilted-incidence zone plate modeling (Ünal 2025) [7] extends the framework to off-axis planetary targets.

2.4 Operating Scales

Near-field ($h_k \sim$ 10–500 m). For $D = 4\,\text{m}$, $H = 100\,\text{m}$, $\lambda = 500\,\text{nm}$, the Fresnel number $\mathcal{F} = D^2/(4\lambda H) \approx 8 \times 10^4$, placing the primary occulting function in the geometric optics regime. Zone-plate lensing acts at scale $r_1 = \sqrt{\lambda H} \approx 7\,\text{mm}$, well within the fabric pixel pitch. Since the DSAS intercepts the wavefront *before* it traverses the lower turbulent boundary layer, only turbulence below h_1 contributes residual seeing.

Stratospheric ($h_k \sim$ 10–15 km). Near the tropopause the atmosphere itself becomes a refractive element. The constructive-interference condition for the accumulated refractive phase is

$$\Delta\phi_{\text{refr}} = \frac{2\pi}{\lambda} \int_{h_1}^{h_K} \bigl[n(h) - 1\bigr]\, dh \approx p\pi, \quad p \in \mathbb{Z}. \tag{5}$$

For standard conditions this integral is $\sim 10^3$ rad at $\lambda = 500\,\text{nm}$ over a 5-km stack. The programmable fabric substrates apply a compensating phase offset at each altitude to satisfy the constructive interference condition (Figure 2).

2.5 Adaptive Optics Integration

The DSAS unifies external starlight suppression with volumetric wavefront sensing. The refractive index at each ring altitude is computed via the modified Edlén formula:

$$n(h_k) - 1 = \frac{77.6 \times 10^{-6}}{T_{\text{atm}}(h_k)} \left[P(h_k) + \frac{4810\, e(h_k)}{T_{\text{atm}}(h_k)}\right], \tag{6}$$

and $C_n^2(h_k)$ is estimated from inter-drone temperature variance fit to the Kolmogorov structure function $D_T(b_{jl}) = C_T^2\, b_{jl}^{2/3}$. The Fried coherence length

$$r_0 = \left[0.423\, k^2 \sec\zeta \int_0^\infty C_n^2(h)\, dh\right]^{-3/5} \tag{7}$$

is updated at 10 Hz as a predictive prior to the deformable mirror (DM) controller.

The embedded photodiode grid constitutes a *distributed Hartmann sensor*. The transport-of-intensity equation

$$\frac{\partial I}{\partial z} = -k\, \nabla_\perp \cdot \bigl(I\, \nabla_\perp \phi\bigr) \tag{8}$$

is evaluated using finite differences between vertically adjacent ring planes, providing a multi-altitude wavefront gradient unavailable to any conventional single-plane sensor. Modal reconstruction in Zernike polynomials yields the feed-forward DM command vector

$$\vec{c}_{\text{DM}} = -\mathbf{M}^\dagger\, \vec{a}, \tag{9}$$

where $\mathbf{M}^\dagger$ is the pseudo-inverse of the DM influence function matrix.

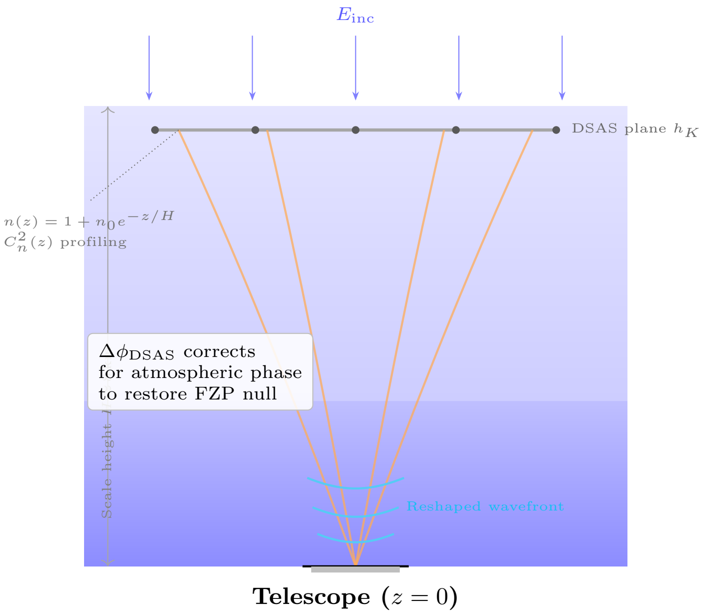

Figure 2: High-altitude (stratospheric) DSAS configuration. Orange rays show the converging wavefront shaped by the multi-plane Fresnel zone plate. Cyan arcs show the coherently reshaped wavefront entering the telescope. The programmable fabric applies a phase correction $\Delta\phi_{\text{DSAS}}$ to counteract atmospheric dispersion and maintain the Fresnel null.

2.6 Optical Vortex Phase Mask

After DSAS suppression and DM correction, residual starlight enters the Optical Vortex Phase Mask (OVPM), which applies the azimuthal phase $e^{il\theta}$ (l even, typically 2 or 4). This creates an on-axis phase singularity that nulls stellar light while leaving any off-axis companion unimpeded (Serabyn 2026) [**?**]. The three-layer cascade—DSAS fabric ($\sim 10^{-4}$), feed-forward DM, OVPM—is projected to achieve the 10^{-10} contrast target.

2.7 Turbulence Mitigation: Tethered Circular Flight

Multi-rotor hover wake is the primary mechanical noise source. We mitigate it by tethering fixed-wing UAVs to the outer rim of each fabric ring and flying them in a continuous banked circular orbit at ≈ 45 bank angle.

Aerodynamic rationale. The horizontal component of lift provides centripetal force; tether tension maintains fabric planarity and radial geometry. The drones fly *outside* the optical clear aperture, shedding their wake vortices radially outward (Figure 3).

Forward-swept wing (FSW). The FSW design (Ngaongam & Ujjin 2024 [8]; Kanazaki & Setoguchi 2023) [9] stalls at the wing root first, keeping ailerons effective at the high angles of attack typical in variable stratospheric winds. Inward spanwise flow concentrates the wake into a narrow, computationally predictable stream that the adaptive optics system can null.

Bioinspired separated-flow airfoil. The Di Luca et al. (2020) [10] sharp-leading-edge design intentionally triggers laminar separation that reattaches consistently before the trailing edge, confining turbulent eddies to the wing's upper surface and away from the Fresnel zone boundaries (Figure 4).

Software counter-rotation. Circular orbital flight rotates the fabric assembly at $\omega(t)$ relative to the celestial target. The programmable substrate compensates by applying the digital transformation

$$T_{\text{active}}(r, \theta, t) = T_{\text{static}}\left(r,\, \theta - \int \omega(t)\, dt\right), \tag{10}$$

keeping the occulting mask and Fresnel zones stationary relative to the star–telescope axis.

Real-time diffraction computation. Achieving 10^{-10} contrast requires evaluating Eq. (1) at 10 Hz. We use the sinc-approximation method of Anderson (2026) [11] and Cubillos & Jimenez (2022) [12], which

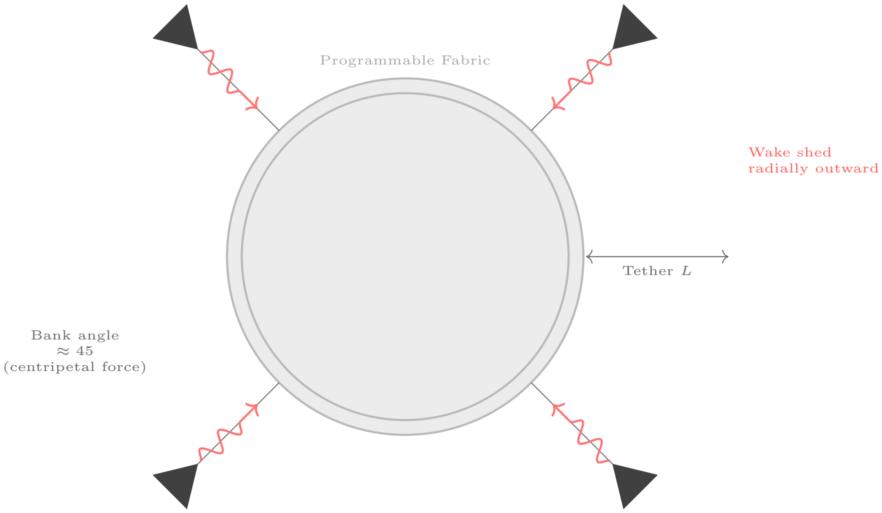

Figure 3: Top-down view of the tethered circular flight configuration. Fixed-wing UAVs (filled triangles) orbit at 45 bank outside the fabric ring. Tether tension (↔) maintains fabric planarity; wake vortices (snake arrows) are shed radially outward, away from the optical axis.

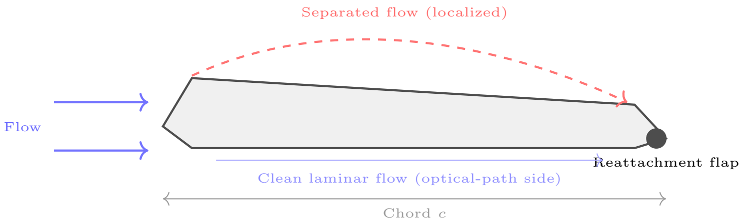

Figure 4: Separated-flow airfoil cross-section (Di Luca et al. 2020) [10]. A sharp leading edge intentionally triggers controlled separation (red dashed arc) that reattaches before the trailing flap. Turbulent eddies are confined to the upper surface; the lower (optical-path) side retains clean laminar flow.

represents $T(x, y)$ as a sinc-function expansion and evaluates the Fresnel integral with substantially lower overhead than FFT or Monte Carlo approaches (Barnett 2021 [13]; Aime et al. 2024 [14]).

3 TNO Occultations as Natural Starshades

3.1 Radial-Velocity Stationary Point Strategy

The apparent angular velocity of a TNO occulter is

$$\omega_{\text{app}} = \frac{v_{\perp,\text{TNO}} - v_{\perp,\text{Obs}}}{d}, \tag{11}$$

where $v_\perp$ is the velocity component perpendicular to the line of sight and d is the observer–TNO distance. For highly eccentric orbits near aphelion, there exist windows where $v_{\perp,\text{TNO}} \approx v_{\perp,\text{Obs}}$. At $d \approx 40\,\text{AU}$, velocity synchronization within $0.1\,\text{km}\,\text{s}^{-1}$ allows the shadow to remain centered on a 6.5-m aperture for several minutes.

3.2 Linear Telescope Array

For TNOs with well-characterized orbits the shadow ground-track can be computed months in advance. A linear array of small fixed telescopes is pre-positioned along the predicted ground-track (Paxman 2021) [15];

GPS-disciplined data acquisition across all elements functions as a single extended exposure with effective integration time

$$t_{\mathrm{eff}} = \frac{L}{v_{\mathrm{track}}}. \tag{12}$$

For $v_{\mathrm{track}} = 5\,\mathrm{km\,s^{-1}}$ and $L = 500\,\mathrm{km}$, this yields $t_{\mathrm{eff}} = 100\,\mathrm{s}$—a window no single station can achieve (Figure 5).

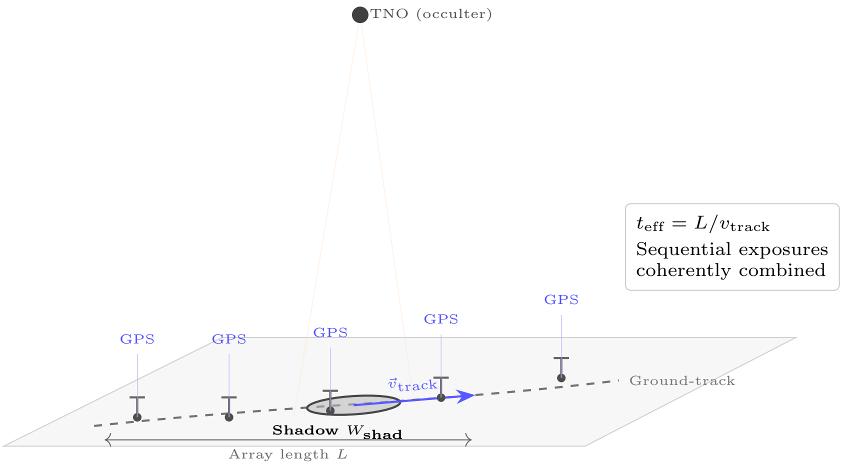

Figure 5: Linear telescope array for TNO occultation integration. Telescopes (vertical T-shapes) are pre-positioned along the predicted shadow ground-track. Each element's GPS-disciplined exposure contributes to a single coherent integration window of duration $t_{\mathrm{eff}} = L/v_{\mathrm{track}}$.

3.3 Irregular Occulter Compensation

If the TNO's shape and spin state are known from prior radar mapping or multi-chord occultation campaigns (e.g., *Arrokoth*/2014 MU_{69}), the Fresnel-Kirchhoff integral

$$U(P) = \frac{Ae^{ikz}}{i\lambda z} \iint_{\Sigma} e^{ik\frac{x^2+y^2}{2z}}\, dx\, dy \tag{13}$$

(Σ = unobstructed area around the TNO) models the wavefront perturbation from irregular limb edges. A pre-computed feed-forward DM (deformable mirror) command pre-adjusts the telescope wavefront as if receiving light from a symmetric occulter, allowing the OVPM (Optical Vortex Phase Mask) to operate at peak efficiency.

4 System Performance

4.1 Contrast Budget

The three-layer suppression cascade is summarized in Table 1. The fabric provides coarse suppression under the assumption of a well-apodized, position-controlled mask (DGPS accuracy $\lesssim$1 cm; fabric surface error $\ll \lambda/4$). The DM feed-forward corrects mid-order atmospheric aberrations using the real-time $C_n^2(h)$ profile. The OVPM provides final nulling under the residual-wavefront errors after DM correction.

4.2 Comparison with JWST

Collecting area. An array of 33 one-meter-class telescopes ($A_{\mathrm{unit}} \approx 0.785\,\mathrm{m}^2$) matches JWST's $\approx$25.4 m^2.

Angular resolution. With a 64-m baseline, $\theta \approx 1.22\lambda/B \approx 7\,\mathrm{mas}$ at $\lambda = 2\,\mu\mathrm{m}$—roughly 10× finer than JWST's 67 mas.

Table 1: Layered contrast budget (projected).

Stage	**Mechanism**	**Contrast**
DSAS fabric	Apodized occultation	$\sim 10^{-4}$
DM feed-forward	C_n^2-guided AO	$\sim 10^{-7}$
OVPM	Phase vortex null	$\sim 10^{-10}$

Integration time. At the Radial-Velocity Stationary Point ($v_{\text{track}} < 1\,\text{km}\,\text{s}^{-1}$), a 64-m array achieves $t_{\text{eff}} \geq 64\,\text{ms}$ per transit event, extendable by the DSAS Fresnel pre-aperture focusing.

Cost. Estimated \$15M–\$50M versus ∼\$10B for JWST (≈200× reduction).

The DSAS does not compete with space-based coronagraphy; it provides a low-cost ground-based pathway to on-sky demonstration of programmable pre-aperture coronagraphy and is best suited to bright, well-characterized nearby stellar systems.

5 Conclusion

We have presented a ground-based architecture for direct exoplanet imaging that distributes the coronagraphic function across a coordinated atmospheric system. The DSAS introduces multi-plane Fresnel zone plate optics as a new degree of freedom in coronagraph design—pre-aperture wavefront shaping decoupled from the sub-nanometer stability requirements of mirror-based instruments. Combined with real-time $C_n^2(h)$ profiling, distributed Hartmann sensing, and an internal OVPM, the system is projected to reach 10^{-10} contrast from the ground. TNO occultations at Radial-Velocity Stationary Points, observed with linear telescope arrays, provide a complementary opportunistic capability requiring no infrastructure beyond portable telescopes. Together, these elements constitute a modular, redeployable system that opens a new experimental pathway toward ground-based direct imaging and spectroscopic characterization of Earth-like exoplanets.

References

[1] Kuhn, E. R., et al. (2025). Drone beam mapping of the TONE radio dish array. *arXiv:2502.03759v2*.
`https://arxiv.org/html/2502.03759v2`

[2] Brown, A. M., Muller, J., de Naurois, M., & Clark, P. (2022). Inter-calibration of atmospheric Cherenkov telescopes with UAV-based airborne calibration system. *Nucl. Instrum. Methods A*.
`https://doi.org/10.1016/j.nima.2022.166370`

[3] Li, J., et al. (2025). Measurement of the primary beam of the Tianlai cylindrical antenna using an unmanned aerial vehicle. *arXiv:2508.01413v1*.
`https://arxiv.org/html/2508.01413v1`

[4] Serabyn, E., & Mawet, D. (2026). Optical vortex phase masks for the detection of habitable worlds. NASA Tech Highlight.
`https://science.nasa.gov/science-research/science-enabling-technology/technology-highlights/optical-vortex-phase-masks-for-the-detection-of-habitable-worlds/`

[5] Shi, C., et al. (2024). Multilevel diffractive lenses: recent advances and applications. *Symmetry*, **16**(10), 1377.
`https://doi.org/10.3390/sym16101377`

[6] Zhang, Z. (2017). Hybrid-level Fresnel zone plate for diffraction efficiency enhancement. *Opt. Express*, **25**, 33676.
`https://doi.org/10.1364/OE.25.033676`

[7] Ünal, A. (2025). Numerical Fresnel models of Fresnel zone plates for plane wave at angle of incidence. *Sci. Rep.*
`https://www.nature.com/articles/s41598-025-92965-y`

[8] Ngaongam, C., & Ujjin, R. (2024). Aerodynamic characteristics of forward swept wing in subsonic speed. *CFD Letters*, ISSN: 2180-1363.
`https://doi.org/10.37934/cfdl.16.5.18`

[9] Kanazaki, M., & Setoguchi, N. (2023). Characteristics of vortices around forward swept wing at low speeds/high angles of attack. *Aerospace*, **10**(9), 790.
`https://doi.org/10.3390/aerospace10090790`

[10] Di Luca, M., Mintchev, S., Su, Y., Shaw, E., & Breuer, K. (2020). A bioinspired separated flow wing provides turbulence resilience and aerodynamic efficiency for miniature drones. *Sci. Robot.*
`https://doi.org/10.1126/scirobotics.aay8533`

[11] Anderson, R. L. (2026). A new tool for evaluating the Fresnel diffraction integral. *Journal for Occultation Astronomy*, JOA 2026-2.
`https://github.com/bob-anderson-ok/Sinc-based-fresnel-diffraction`

[12] Cubillos, M., & Jimenez, E. (2022). Diffraction integral computation using sinc approximation. *Appl. Numer. Math.*, **178**.
`https://doi.org/10.1016/j.apnum.2022.02.011`

[13] Barnett, A. H. (2021). Efficient high-order accurate Fresnel diffraction via areal quadrature and the nonuniform fast Fourier transform. *JATIS*, **7**(2), 021211.
`https://doi.org/10.1117/1.JATIS.7.2.021211`

[14] Aime, C., Prunet, S., Theys, C., Ferrari, A., & Lantéri, H. (2024). A new approach for the numerical calculation of diffraction patterns using starshades. *A&A*.
`https://doi.org/10.1051/0004-6361/202449589`

[15] Paxman, R., et al. (2021). Synthetic-aperture silhouette imaging (SASI): laboratory demonstration traceable to ground-based imaging of GEO satellites. *COSI 2020 Proc.*
`https://doi.org/10.1364/COSI.2020.CTh4C.6`

[16] Damiano, M., et al. (2024). Starshade exoplanet data challenge: what we learned. *arXiv:2410.09183*.
`https://arxiv.org/abs/2410.09183`